Raman spectroscopy of transition metal dichalcogenides

2016 J. Phys.: Condens. Matter 28 353002

(http://iopscience.iop.org/0953-8984/28/35/353002)

IOP Publishing Journal of Physics: Condensed Matter
J. Phys.: Condens. Matter **28** (2016) 353002 (16pp) doi:10.1088/0953-8984/28/35/353002

Topical Review

Raman spectroscopy of transition metal dichalcogenides

R Saito[1], Y Tatsumi[1], S Huang[2], X Ling[2] and M S Dresselhaus[2,3]

[1] Department of Physics, Tohoku University, Sendai 980-8578, Japan
[2] Department of Electrical Engineering and Computer Scienece, Massachusetts Institute of Technology, Cambridge, MA 02139, USA
[3] Department of Physics, Massachusetts Institute of Technology, Cambridge, MA 02139, USA

E-mail: rsaito@flex.phys.tohoku.ac.jp

Received 30 March 2016, revised 19 May 2016
Accepted for publication 23 May 2016
Published 7 July 2016

Abstract

Raman spectroscopy of transition metal dichalcogenides (TMDs) is reviewed based on our recent theoretical and experimental works. First, we discuss the semi-classical and quantum mechanical description for the polarization dependence of Raman spectra of TMDs in which the optical dipole transition matrix elements as a function of laser excitation energy are important for understanding the polarization dependence of the Raman intensity and Raman tensor. Overviewing the symmetry of TMDs, we discuss the dependence of the Raman spectra of TMDs on layer thickness, polarization, laser energy and the structural phase. Furthermore, we discuss the Raman spectra of twisted bilayer and heterostructures of TMDs. Finally, we give our perspectives on the Raman spectroscopy of TMDs.

Keywords: Raman spectroscopy, polarization dependence, Raman tensor, transition metal dichalcogenides, group theory

(Some figures may appear in colour only in the online journal)

1. Introduction

Layered transition metal dichalcogenides (TMDs) are mostly MX_2 compounds having a structure with each constituent trilayer consisting of a central layer of metallic atoms (M = Mo, W, Nb, Ta) sandwiched between two chalcogen atom layers (X = S, Se, Te). Although TMDs exist as natural mineral products and have been widely used for many years for industrial applications, such as lubricant materials for combustion engines, the newly emerging science of atomic layer TMDs was investigated significantly only after the rise of graphene in 2004 [1].

Graphene and TMDs are typical two-dimensional (2D) atomic layered materials which can be obtained by the exfoliation from their bulk three-dimensional (3D) materials using the scotch tape method [1] or by direct synthesis using chemical vapor deposition (CVD) [2]. Since graphene is a semi-metal, semiconducting and insulating atomic layers are needed in order to fabricate a semiconductor device by combining different atomic layer materials. TMD atomic layers include diverse members from metallic to semiconducting, which are considered to be the basic units for constructing building blocks of artificial new materials. By stacking TMD members together with different energy band alignments and doping types, we can achieve desirable properties for specific electronic and optoelectronic devices. This gives more freedom to engineer novel 2D heterostructures which are not found in nature.

However, there are some challenges to be addressed when characterizing the stacked TMD layers, mainly due to the following reasons: (1) many possible structures: the stacking is not generally epitaxial or unique, but has a rotational (or translational) freedom with reference to an axis perpendicular to (or also along) a 2D plane; (2) observation of the weak interlayer interaction: the interaction between two adjacent TMD layers is much smaller than the intralayer interaction within

the constituent layers of the trilayer; (3) observation of inner layers: the physical properties of each layer within the stacked TMDs are not selectively accessible except for the outermost layer.

Comparing to other characterization tools, Raman spectroscopy provides a quick, convenient, nondestructive and non-invasive method for characterizing the 2D materials with high selectively for the interior layers [3–6]. Measurements can be made at room temperature and at ambient pressure without complicated sample preparation processes. Raman scattering involves the inelastic scattering of the incident light in a material, where the energy of the scattered light either decreases by exciting an elementary excitation of the solid material (i.e. a phonon) or increases by absorbing a phonon. Raman spectra give the intensity of the scattered light as a function of the energy shift from the incident light (Raman shift). The typical accuracy of measurements of Raman spectra is $1\,\mathrm{cm}^{-1}$ (~0.1 meV) which is sufficient for measuring the interlayer interaction (several meV) of TMDs. Raman spectroscopy has been widely used and has become a standard characterization technique for TMDs, graphene and other atomic layer materials [4]. In this article, we discuss how to observe the TMDs and related atomic layer materials by Raman spectroscopy.

There are several advantages of using Raman spectroscopy for the characterization of low dimensional materials, including 2D TMDs [7, 8]. One reason is that the electronic density of states (DOS) has a so-called van Hove singularity [4], which leads to a strong Raman feature when the photon energy is matched to the van Hove singularity of the DOS for each layer. This special case is known as resonance Raman scattering. If we have many laser sources available for an experiment and if we measure the Raman intensity as a function of laser energy (that is called a Raman excitation profile), we can see this resonance Raman effect clearly by probing the van Hove singularity [9]. By using resonance Raman spectroscopy, we can thus obtain not only phonon frequency information for each material but also electronic energy band information which is sensitive to the strain in the materials [10]. In addition, by changing the laser excitation energy, we can selectively distinguish each layer of different layered materials, as they have different characteristic resonant conditions, thereby gaining deeper understanding of the physical principles that are involved.

The second advantage is that more specific selection rules predicted from the group theory applicable to the particular optical transition can be applied to many TMD layered materials with lower symmetry compared to graphene, as discussed in this paper. In this way, differences in symmetry distinguish the spectral features of a particular TMD layer from another layer, and from another TMD with different symmetry. Furthermore, by focusing the laser light in a confocal optical microscope, we can measure a high spatially resolved Raman signal (about one micron). By scanning focused laser light on the TMDs, we can get so-called Raman imaging maps [11, 12] which could provide detailed information about the characteristic defects of the particular crystal structure over a relatively large area in comparison to high-resolution transmission electron microscope studies. Therefore, added information may often be efficiently obtained by using multiple techniques on an individual grown sample or on a specially grown group of samples, specially designed to study a particular effect.

In addition, in the optical transitions involved in the so-called Raman process, the optical dipole selection rule restricts the possible electronic transitions and the possible Raman-active phonon modes, which could be sensitive to the number of atomic layers and to the laser polarization direction [13, 14]. In this article, we will show some examples of TMDs and related materials in which we demonstrate how to analyze the Raman spectra combined with theory, and with other complementary experimental probes, as appropriate.

The organization of this paper is as follow. In section 2, we discuss how the polarization dependence and the dipole selection rules appear in the Raman intensity formula both for the semi-classical and quantum mechanical approaches. In section 3, we show the dependence of TMD Raman spectra on various parameters, including the number of layers, the laser excitation wavelength and polarization, and the structural phase. We consider both model materials for clarifying the fundamental physics principles and specific physical systems to illustrate recent advances in this field of study. In section 4, we will discuss the application of Raman spectra in studying the interlayer coupling of the TMDs heterostructures. Section 5 is devoted to a summary of the present status of this field and looking toward to the future.

2. Classical and quantum description for polarized Raman intensity

2.1. Raman tensor of TMD

In polarized Raman spectroscopy studies, we measure the intensity of the scattered light as a function of the polarization direction of both the incident and scattered light independently. If the polarization directions of the incident and scattered light are parallel to each other, the scattering process is called parallel polarization. In the parallel polarization geometry (see figure 1(a)), we generally see the so-called A_1 (or A_{1g}) phonon which is Raman-active. Here, A_1 or A_{1g} are labels of the irreducible representations of a point group for which we know the labels and the corresponding functions for the irreducible representations from the character table for the symmetry group that is involved. In the character table of a given symmetry group, such as C_{2v} or T_d etc., we can see how many irreducible representations are in the group. Group theory tells us whether the irreducible representation whose basis function behaves as a quadratic term of x, y, z, such as $x^2 + y^2$ or xy etc. is, or is not a Raman-active mode. This statement can be understood by the classical formula [15] for the Raman intensity, I,

$$I = \left|{}^{t}\boldsymbol{e}_{s} R \boldsymbol{e}_{i}\right|^{2}, \tag{1}$$

where $\boldsymbol{e}_i$ and $\boldsymbol{e}_s$ are, respectively, unit vectors of the electric field for the incident and scattered light and the superscript t of $\boldsymbol{e}_s$ denotes the transformation from a column vector to a row vector. R describes a second rank tensor called the Raman tensor, and R is transformed by the unitary transformation

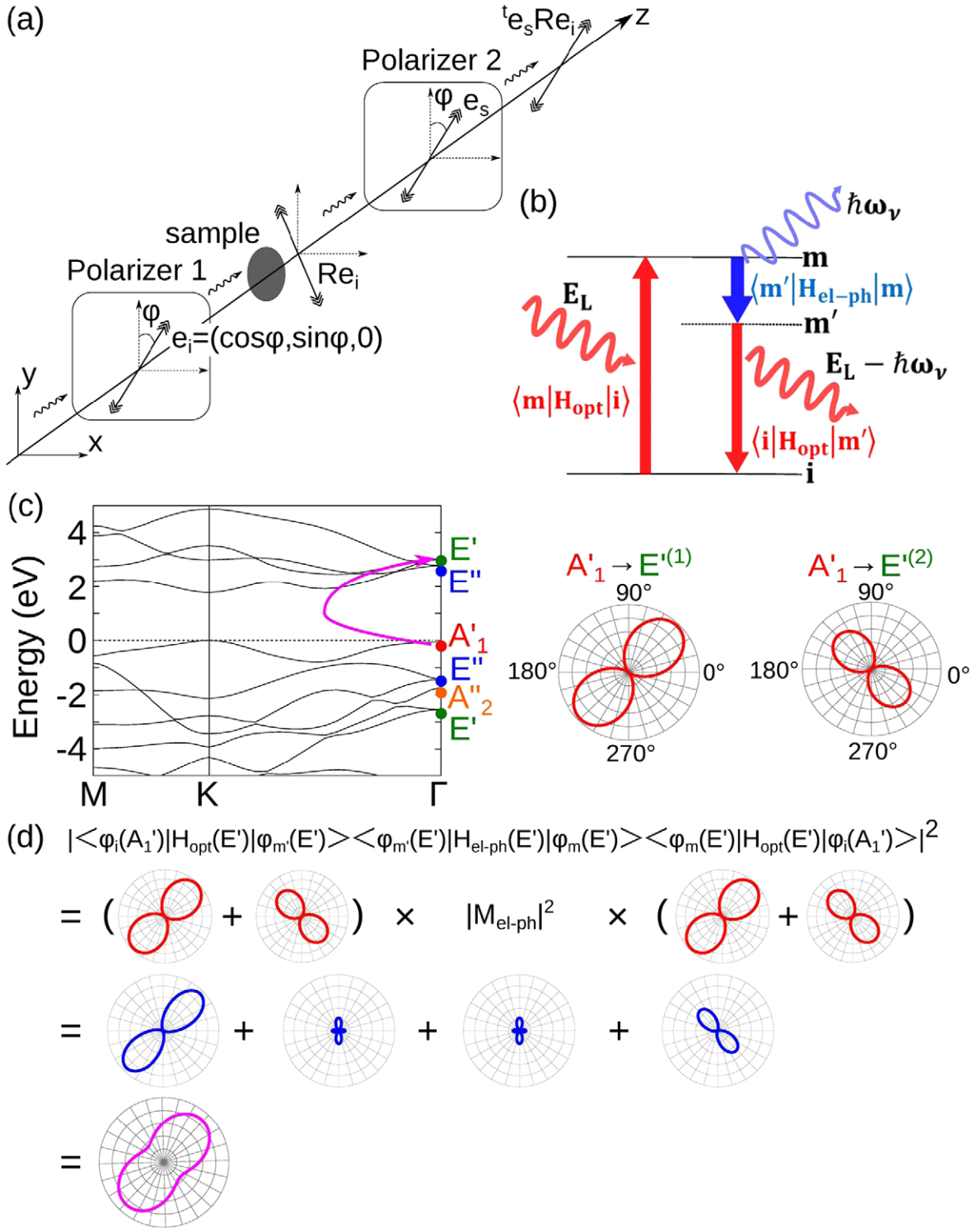

Figure 1. (a) Polarized Raman spectra are observed by rotating the two polarizers 1, and 2 for the incident and scattered light independently. In the figure, we show the parallel polarization (b) Raman scattering process, in which E_L is the optical light source and $\hbar\omega_\nu$ is the phonon frequency; and i, m, and m' denote, respectively, the initial, intermediate, and scattered states; H_{opt} ($\propto \mathbf{A}\cdot\nabla$) and H_{el-ph} denote the optical and electron–phonon interactions. (c) Energy bands of monolayer MoS_2 and the assignment of symmetry for the wave functions at the Γ point. The polar plots of the intensity for the electron–photon interaction matrix elements between A_1' and two E' electronic states are also shown. (d) Polar plots of the Raman intensity for the E' mode at the Γ point, obtained by the multiplication of two electron–photon matrix elements. We assume no anisotropy for the electron–phonon interaction.

$U^{-1}RU$ for a given rotation U of coordinate axis, which is the definition of the second-rank tensor. The Raman tensor is represented by a 3 by 3 matrix and $R\boldsymbol{e}_i$ corresponds to the scattered light polarization for a given incident light polarization $\boldsymbol{e}_i$ as shown in figure 1(a). The scattered amplitude observed in the direction of $\boldsymbol{e}_s$ is given by the inner product of

Table 1. Character table for D_{3h} point group for an odd number of TMD layers.

	E	$2C_3$	$3C_2'$	σ_h	$2S_3$	$3\sigma_v$	Linear, rotations	Quadratic	Optical activity
A_1'	1	1	1	1	1	1		x^2+y^2, z^2	R
A_2'	1	1	−1	1	1	−1	R_z		
E'	2	−1	0	2	−1	0	(x, y)	(x^2-y^2, xy)	$IR+R$
A_1''	1	1	1	−1	−1	−1			
A_2''	1	1	−1	−1	−1	1	z		IR
E''	2	−1	0	−2	1	0	(R_x, R_y)	(xz, yz)	R
$\Gamma_{a.s.}$	3	3	1	1	1	3	a.s. = atomic sites		
Γ_{xyz}	3	0	−1	1	−2	1	$E'+A_2''$		
$\Gamma_{vib.}$	9	0	−1	1	−2	3	$A_1'+2E'+2A_2''+E''$		

$\boldsymbol{e}_s$ and $R\boldsymbol{e}_i$ as shown in equation (1). If there is no polarizer in the path of the scattered light, the intensity is given by $|R\boldsymbol{e}_i|^2$.

Here R represents the vibrating transition dipole moment (i.e. the dipole moment induced by the optical absorption) with a phonon frequency ω_{ph} [16]. When the incident light with photon frequency ω_L is to be coupled with R having a phonon frequency ω_{ph}, we get inelastic scattered light with a beat frequency of either a downshifted $\omega_{L-}\ \omega_{ph}$ (Stokes shift) or an upshifted $\omega_{L+}\ \omega_{ph}$ (anti-stokes shift) phonon response. In order to get a non-zero intensity I signal, R has a non-zero matrix element for the Raman tensor R which depends on the irreducible representation of the phonon modes. The Raman spectra are observed when I becomes non-zero for the given $\boldsymbol{e}_i$ and $\boldsymbol{e}_s$ used in our experiment. The information for the Raman-active modes and the direction of $\boldsymbol{e}_i$ and $\boldsymbol{e}_s$ can be obtained by the character table which is special for each materials system under investigation.

For example, in table 1, we show the character table for the D_{3h} point group, to which odd numbers of TMD layers belong. Suppose that $\boldsymbol{e}_i$ is in the direction of x whose irreducible representation is E', and $\boldsymbol{e}_s$ in y (E') that corresponds to cross polarization, then R should belong to the irreducible representation of xy (E') in order to get the product $y*xy*x=x^2y^2$ which becomes an even function of x or y. If the product is an odd function of x or y, I becomes negative for $-x$ or $-y$ so that I becomes zero. Since the irreducible representation E' has a function of xy, then the phonon with the symmetry of E' is Raman-active for the given geometry of cross polarization $\boldsymbol{e}_i$ and $\boldsymbol{e}_s$. For parallel polarization, $\boldsymbol{e}_i=\boldsymbol{e}_s=x$ (or y), but on the other hand, the E', xy phonon is not Raman active, while (x^2+y^2), or z^2 (A_1'), or x^2-y^2 (E') is Raman active. Thus if we observe a Raman signal for parallel polarization but not for cross polarization, the symmetry of the phonon is A_1'. If we observe a Raman signal both for parallel and cross polarization, then the symmetry of the phonon is E' and Raman active. It is noted that the symmetry labels for the phonon mode can be assigned theoretically by projecting the so-called projection operator of the E' irreducible representation onto the phonon displacement vector [17]. If the projected result becomes zero (the identity), the displacement does not (does) belong to E'. The shapes of the Raman active R matrices discussed here are expressed as

$$R(E', xy)=\begin{pmatrix}0&d&0\\d&0&0\\0&0&0\end{pmatrix},\quad R(E',\ x^2-y^2)=\begin{pmatrix}c&0&0\\0&-c&0\\0&0&0\end{pmatrix},$$
$$R(A_1',\ x^2+y^2 \text{ and } z^2)=\begin{pmatrix}a&0&0\\0&a&0\\0&0&b\end{pmatrix}. \tag{2}$$

The shape of the R matrix for the E', xy phonon can be determined such that the xy (and yx) matrix element of R becomes non-zero. For the E', x^2-y^2 phonon, the diagonal terms for x and y have the same value with opposite signs. For the A_1' phonon, the diagonal matrix element of R becomes non-zero as shown in equation (2). For the remaining Raman modes (E'') of the D_{3h} point group or the other point groups of TMDs, the shape of R can be seen in [7], which can be obtained by ourselves once we know the physical situation.

2.2. Classical theory of the polarization dependence

The classical theory of the polarized Raman spectra is useful for understanding the polarization dependence of the Raman intensity for a given incident laser energy geometry. Let us show a simple example for the polarization dependence of the E', xy phonon. The linear polarized light for the scattered wave $\boldsymbol{e}_s$ in the direction within the xy plane with an angle φ measured from the x axis (the propagating direction is z) is given by (see figure 1(a))

$$\boldsymbol{e}_i=\begin{pmatrix}\cos\varphi\\\sin\varphi\\0\end{pmatrix}. \tag{3}$$

In the parallel polarization geometry ($\boldsymbol{e}_i=\boldsymbol{e}_s$), from equations (1)–(3) the polarization dependence of E' phonon is given by

$$I=\left|(\cos\varphi\ \sin\varphi\ 0)\begin{pmatrix}0&d&0\\d&0&0\\0&0&0\end{pmatrix}\begin{pmatrix}\cos\varphi\\\sin\varphi\\0\end{pmatrix}\right.$$
$$\left.+(\cos\varphi\ \sin\varphi\ 0)\begin{pmatrix}c&0&0\\0&-c&0\\0&0&0\end{pmatrix}\begin{pmatrix}\cos\varphi\\\sin\varphi\\0\end{pmatrix}\right|^2$$
$$=|d\sin 2\varphi+c\cos 2\varphi|^2, \tag{4}$$

where we particularly assume an interference effect of the two scattered amplitudes of the Raman tensors between $R(E', xy)$ and $R(E', x^2 - y^2)$. In general, inelastic scattered light loses the phase information of the incident light and thus the interference effect between the two different phonon modes is not observed. However, when the materials are sufficiently thin compared with the wavelength of the laser light, two independent inelastic scattering processes occur almost at the same time by emitting a phonon with the different modes but with the same energy (E' mode). In such a case, the interference between the two scattered light modes can be expected to occur. If the interference does not occur, equation (4) would give $d^2 \sin^2 2\varphi + c^2 \cos^2 2\varphi$. Further, if we assume that $d \cong c$, no polarization effect might appear, which we generally see in the discussion in published works [7]. It would, however, be interesting to measure the coherent polarization dependence by selecting a special geometry for the experiment, which allows direct observation of this interference effect, as is done in the present work.

2.3. Quantum description of the Raman tensor

In the previous section, we discussed the polarization dependence with a fixed value of the laser energy E_L. However, when we change E_L, we can no longer use the above classical theory for the polarization dependence which is independent of laser energy, since the discussion of the optical dipole selection rule for photon absorption and emission is not included in the classical theory. For Stokes Raman scattering, there are three sub-processes in a Raman process; (1) photon absorption, (2) phonon emission, and (3) photon emission, which are schematically shown in figure 1(b). In the quantum theory, the dipole selection rule for optical transitions is expressed in the Raman intensity formula which is given by,

$$I = \left| \sum_{i,m,m'} \frac{\langle f|\nabla|m'\rangle \langle m'|H_{\text{el-ph}}|m\rangle \langle m|\nabla|i\rangle}{(E_L - \Delta E_{mi})(E_L - \hbar\omega_\nu - \Delta E_{m'i})} \right|^2 \qquad (5)$$

where $\langle m|\nabla|i\rangle$ and $\langle f|\nabla|m'\rangle$ correspond to the electron–photon interaction of the optical absorption (emission) and $\langle m'|H_{\text{el-ph}}|m\rangle$ is the electron–phonon interaction matrix element for emitting a phonon [4], ω_ν is the frequency of an emitted phonon, and $\Delta E_{mi} \equiv E_m - E_i + i\Gamma$ is the differences of energies between initial and intermediate states with a spectral width Γ due to the uncertainly principle. It is noted that the final electronic state f should be identical to the initial state i so as to show that the electron has recombined with a hole. If we neglect higher order multipole or non-linear effects in the interaction of light with an electron, the perturbation Hamiltonian for the electron–photon interaction is given by the inner product of $\mathbf{A}\cdot\nabla$ [18] where $\mathbf{A}$ denotes the vector potential associated with light and the direction of $\mathbf{A}$ is parallel to the polarization vectors of the electric field $\boldsymbol{e}_i$ and $\boldsymbol{e}_s$ for both the incident and scattered light. Usually the electronic wavefunctions of the initial and intermediate states are much smaller compared with the wavelength of the light, so that $\mathbf{A}$ in the integration of $\langle m|\mathbf{A}\cdot\nabla|i\rangle$ can be taken as a constant as a first approximation and we can assume that $\langle m|\mathbf{A}\cdot\nabla|i\rangle = \mathbf{A}\cdot\langle m|\nabla|i\rangle$, which is called the dipole-approximation [19]. Thus when we consider the direction of $\mathbf{A}$ for both the incident and the scattered light $\boldsymbol{e}_i$ and $\boldsymbol{e}_s$, we can compare equations (5) with (1) and we can understand that the Raman tensor R in equation (1) can be expressed by two electron–photon matrix elements for the incident photon absorption and the scattered photon emission processes and one electron–photon matrix element in which a photo-excited electron emits one phonon. Here we can use group theory for each matrix element. For example, for $\langle m|\nabla|i\rangle$, if the product of three irreducible representations of i, m, and ∇ belongs to the A_1' of D_{3h}, the integration becomes non-zero which is associated with the dipole selection rule [17]. Similarly for the electron–photon interaction $\langle m'|H_{\text{el-ph}}|m\rangle$, if the product of the three irreducible representations of m, m' and $H_{\text{el-ph}}$ (that is the irreducible representation of the phonon mode) belongs to the A_1' representation, the integration becomes non-zero and the phonon mode becomes Raman active for the given intermediate states.

In figure 1(c), we show the energy bands of monolayer MoS_2 with the labels of the irreducible representations for the wavefunctions at the Γ point. In figure 1(c) we also show two polar plots of the intensity for the electron–photon interaction matrix elements between A_1' and two E' electronic states. Here we assumed that the two processes of $A_1' \rightarrow E'^{(1)}$ and $A_1' \rightarrow E'^{(2)}$ do not interfere with each other. It is important to note that the two polar plots give not only different maximum angles but also different values of the maximum intensity. The two polar plots of the electron–photon matrix elements appear in the Raman intensity formula for the phonon mode E' as shown in figure 1(d). When we assume that the electron–photon interaction for the E' phonon does not show any anisotropy, the polarization dependence of the Raman intensity for the E' phonon is given by the sum of the four terms of polar plots as shown in figure 1(d).

When we compare equations (2) with (5), the xy component d of the Raman tensor $R(E', xy)$ in equation (2) for given m and m' states in equation (5) can be expressed by

$$d \propto \begin{cases} \dfrac{\left\langle f|\frac{\partial}{\partial x}|m'\right\rangle \langle m'|H_{\text{el-ph}}|m\rangle \left\langle m|\frac{\partial}{\partial y}|i\right\rangle}{(E_L - \Delta E_{mi})(E_L - \hbar\omega_\nu - \Delta E_{m'i})} & (\boldsymbol{e_i} = \boldsymbol{x},\ \boldsymbol{e_s} = \boldsymbol{y}) \\ \dfrac{\left\langle f|\frac{\partial}{\partial y}|m'\right\rangle \langle m'|H_{\text{el-ph}}|m\rangle \left\langle m|\frac{\partial}{\partial x}|i\right\rangle}{(E_L - \Delta E_{mi})(E_L - \hbar\omega_\nu - \Delta E_{m'i})} & (\boldsymbol{e_i} = \boldsymbol{y},\ \boldsymbol{e_s} = \boldsymbol{x}) \end{cases} . \qquad (6)$$

The upper term of equation (6) corresponds to the case of $\boldsymbol{e}_i = \boldsymbol{x}, \boldsymbol{e}_s = \boldsymbol{y}$, while the lower term corresponds to the case of $\boldsymbol{e}_i = \boldsymbol{y}, \boldsymbol{e}_s = \boldsymbol{x}$. From equation (6), we can guess $d \neq c$ in equation (2) and that both d and c are E_L dependent.

Further, for a given laser energy, we should take the sum for the i, m, and m' states for equation (6) in which the resonance states that give the smaller energy denominator of equation (6) give the main contribution of d. When the energy of the incident light changes, the intermediate state, m, changes to a new state m_{new} to make the energy denominator smaller. Then, the theoretical dipole matrix element has a new dipole selection rule, and we may get a different polarization dependence

Table 2. The space and point groups of TMD materials with different phases and thicknesses ('−' denotes either no structure or no presently available data).

Material	Phase	Space group	Point group		
		Bulk	N = odd	N = even	Bulk
MoS_2, $MoSe_2$, WS_2, WSe_2, $MoTe_2$, $SnSe_2$	2H	$P6_3\,mmc^{-1}$	D_{3h}	D_{3d}	D_{6h}
	1T	$P\bar{3}m1$	D_{3d}	D_{3d}	D_{3d}
	3R	R3m	—	—	C_{3v}
	1T′	$P2_1\,m^{-1}$	—	—	—
WTe_2	1T′	$Pnm2_1$	—	—	—
$ReSe_2$, ReS_2	1T′	$P\bar{1}$	—	—	C_i

of the optical absorption (emission) and Raman intensity. Further for m_{new}, the possible phonon mode that gives a non-zero $\langle m'|H_{el-ph}|m'\rangle$ matrix element might be changed. Such a situation may frequently happen for TMD materials or black phosphorous [14] in which many energy bands with different symmetries exist within a relatively small range of energy. It is important to note that the relative energy position of many intermediate states can be exchanged by changing the layer thickness, which is the reason why we get different polarization plots for the same Raman spectra by changing the thickness [12]. Thus the analysis of the polarization dependence of TMD materials is not easy for low dimensional phenomena without detailed theoretical analysis. Hereafter we will demonstrate these complexities by showing typical examples below, where symmetry is used with special care. By showing the examples that we have investigated so far, we will discuss in the present study what we can learn about low symmetry materials from spectroscopy experiments.

3. Typical Raman spectral features of TMDs

3.1. Different symmetries in TMD materials

There are many TMD materials, with different crystal structures [20–22] as shown in table 2, which are classified in this section. Bulk 2H-MoS_2, WS_2, $MoSe_2$, WSe_2 have high symmetry with the point group D_{6h}, while bulk ReS_2, and $ReSe_2$, have lower symmetry with the point group C_i. In the case of layered TMDs, the symmetry changes from that of a bulk layered material as a function of the number of layers. For example, the 2H-MoS_2 stacking arrangement has space group D^4_{6h} and point group D_{6h} for its bulk phase, but the point group is reduced to D_{3h} or D_{3d} for odd or even numbers of layers, respectively. Further, the symmetry can be changed by changing the phase of the structures from 2H to 1T, such as occurs for the point group D_{3d} for 1T-TaS_2, 1T-MoS_2.

Figure 2(a) illustrates the three phases of structures in TMDs: 2H, 3R and 1T. The 1T′ phase under some conditions experiences a lattice reconstruction from the 1T structure to the 1T′ structure in which the symmetry becomes lower so as to get a more stable structure, as shown in figure 2(b), occurs in $MoTe_2$ [55]. For a given symmetry of the TMD material, the number of Raman active or infrared (IR) active modes can be calculated by the character tables for the crystal symmetry that is stabilized [17]. Raman or IR active modes belong to the irreducible representations of the appropriate point groups which have quadratic terms such as xy, $x^2 - y^2$ etc. or linear term such as x, y, z, respectively. For example, when we see the case of the D_{3h} (table 1), A'_1 ($x^2 + y^2$, z^2), E' ($x^2 - y^2$, xy), and E'' (xz, yz) are Raman active modes, while E' (x, y), and A''_2 (z) are IR active modes. Since D_{3h} does not have an inversion operator, E' can be both Raman and IR active. In general if there is an inversion operator in a point group, the irreducible representations of the group are either even (g, so that the corresponding phonon mode can be Raman active) or odd (u, IR active) basis functions. The number of the Raman-active modes can be obtained by decomposing the reducible representations of the product of $\Gamma_{a.s.} * \Gamma_{xyz}$ into irreducible representations in which $\Gamma_{a.s.}$ and Γ_{xyz} are, respectively, the reducible representations of the so-called atomic sites (number of atoms in the unit cell that do not change their position for a given symmetry operation) and a (x,y,z) translation [17]. In table 1, we show the values of $\Gamma_{a.s.}$ and Γ_{xyz} which gives Raman active modes $A'_1 + 2E' + E''$, and IR modes $2E' + A''_2$. Thus if we measure both the Raman and IR active modes, the spectra that can be observed in both the Raman and IR modes correspond to $2E'$, and other spectra can be assigned to irreducible representations combined with other polarization dependences of the spectra.

Odd or even numbers of layers of a TMD can lead to different symmetry labels and numbers of Raman modes. For example, the E_{1g}, E^1_{2g} and A_{1g} modes for bulk MoS_2 are notated by E' and E'' and A'_1 for odd numbers of layers, or as E^2_g, E^1_g and A_{1g} for even numbers of layers, respectively [23]. Further, the frequencies of the Raman active modes of multilayer TMDs can be shifted from the values for the monolayer or bulk TMDs because of the weak interlayer interactions. For example, the E_{2g} and A_{1g} modes of MoS_2 undergo blue and red shifts as the thickness decreases from bulk to few layers, leading to a frequency difference of the E_{2g} and A_{1g} modes that can be as large as $20\,cm^{-1}$ for monolayer MoS_2 and $25\,cm^{-1}$ for bulk MoS_2 [24, 25]. Most TMD materials with the D_{6h} symmetry are semiconducting in their 2H phase, such as MoS_2, $MoSe_2$, WS_2, WSe_2, and $MoTe_2$ [26]. For all these materials, the 2H phase is much more stable energetically than the 1T and 1T′ phases. Among the D_{6h} TMDs, for MoS_2, $MoSe_2$, WS_2, and WSe_2, their 2H phase is much more stable than their 1T′ phase, while for $MoTe_2$, the 2H phase is only slightly more stable than the 1T′ phase by no more than 0.1 eV per MX_2 unit cell [27, 28]. Thus the 1T′ phase of $MoTe_2$ can be observed

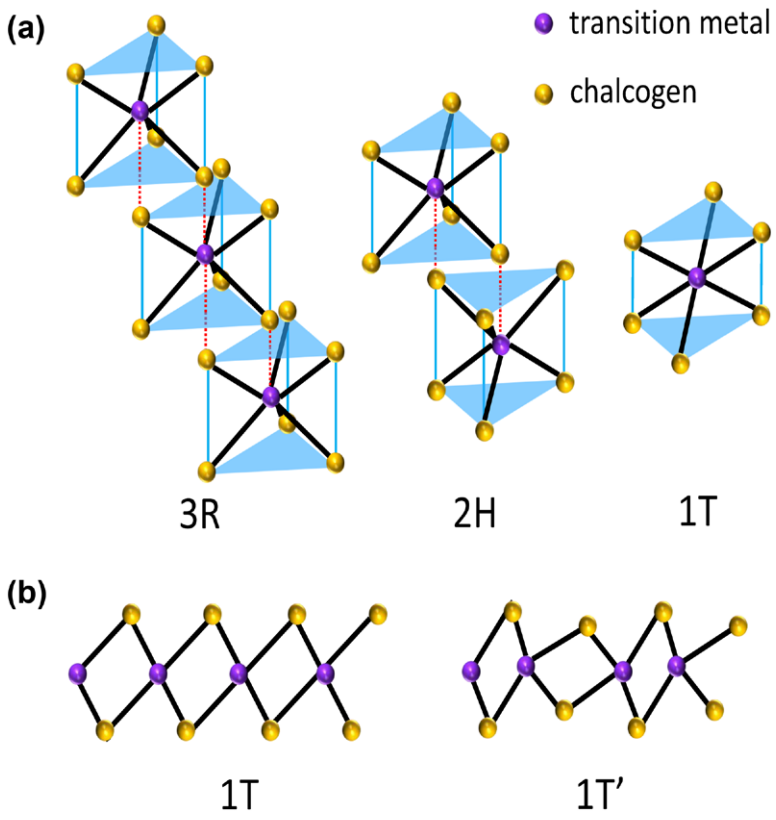

Figure 2. (a) Three phases of D_{6h} TMDs: 3R, 2H and 1T. (b) Top view for structures with the 1T and 1T′ phases.

from room temperature and up to a high temperature of 570 K [29]. Another material, WTe_2, appears to have the 1T′ phase at room temperature, since its 1T′ phase is more stable than the 2H phase. Therefore, WTe_2 is typically an orthorhombic structure with the space group $Pnm2_1$. For 2H MoS_2, $MoSe_2$, WS_2, and WSe_2, their monolayer structures have a direct bandgap, while bilayer to bulk are all indirect bandgap semiconducting materials [30, 31]. Their 1T phases are all semi-metals. Existence of two phases within the same material is useful for electrical applications. For example, the 2H − 1T(1T′) junction can be used for electronic applications, taking advantage of their low contact resistance insofar as the electrodes can be made of the same chemical species [32].

$SnSe_2$ is another TMD material with a hexagonal structure and its bulk phase has D_{6h} symmetry [33]. It is an *n*-type semiconductor, and its small bandgap of around 1.0 eV makes it desirable for applications, including infrared optoelectronic devices [33], solar cells [34], phase change memories [35], and battery anodes [36]. $SnSe_2$ can also be evolved into SnSe which has an orthorhombic structure [37], and the 2H −1T(1T′) phases of SnSe offer the opportunity for flexibly controlling and for mapping systems with tunable properties that are desirable for use in various practical applications [37].

Besides, some other TMD materials, such as the 1T phase of TaS_2, $TaSe_2$ and VSe_2 have shown a charge-density wave (CDW) phase transition [38, 39]. The only TMD material with metallic properties in the 2H phase is NbS_2 [40]. While NbS_2 in the 2H phase does not show a CDW phase transition [41, 42], NbS_2 in the 3R phase shows a CDW phase transition [43]. Moreover, NbS_2 and $NbSe_2$ both show superconductivity below a critical temperature and pressure [40, 44].

The TMD materials with the lowest symmetry are $ReSe_2$ and ReS_2, which have space group $P\bar{1}$ and point group C_i in their bulk phases. In this low symmetry group, only one symmetry operation: a center of inversion remains. $ReSe_2$ has some of the heaviest elements of the TMD family, and can, therefore, also show strong spin–orbit splitting effects. Unlike some common TMDs, such as MoS_2, the $ReSe_2$ crystal contains not only metal–chalcogen bonds but also metal–metal bonds. For any number of layers, $ReSe_2$ and ReS_2 have indirect and direct bandgaps, respectively. Therefore, the interlayer coupling in $ReSe_2$ and ReS_2 is generally weaker than it is in some other TMDs, such as in the common MoS_2 and WSe_2 [45]. In fact, the bulk forms of ReS_2 and $ReSe_2$ resemble their monolayer properties in many ways, including their electronic and optical properties, due to their special charge decoupling. Therefore, the study of those bulk materials can further reveal details about the special properties of few-layer ReS_2 and $ReSe_2$ [45, 46]. Due to its low symmetry, there is strong in-plane anisotropy in $ReSe_2$, which is observed in its various properties, including Raman scattering [47–49] and its electrical and optical properties [50–52].

For all of the layered materials discussed in this review article, including the layered TMDs, there are two typical categories of Raman vibrations that we look for. One occurs within a layer, and is called intralayer vibrations. These vibrations give the intralayer Raman modes which normally appear in the high-frequency region of the spectra. Another type of vibration involves the relative motion of the layers, which

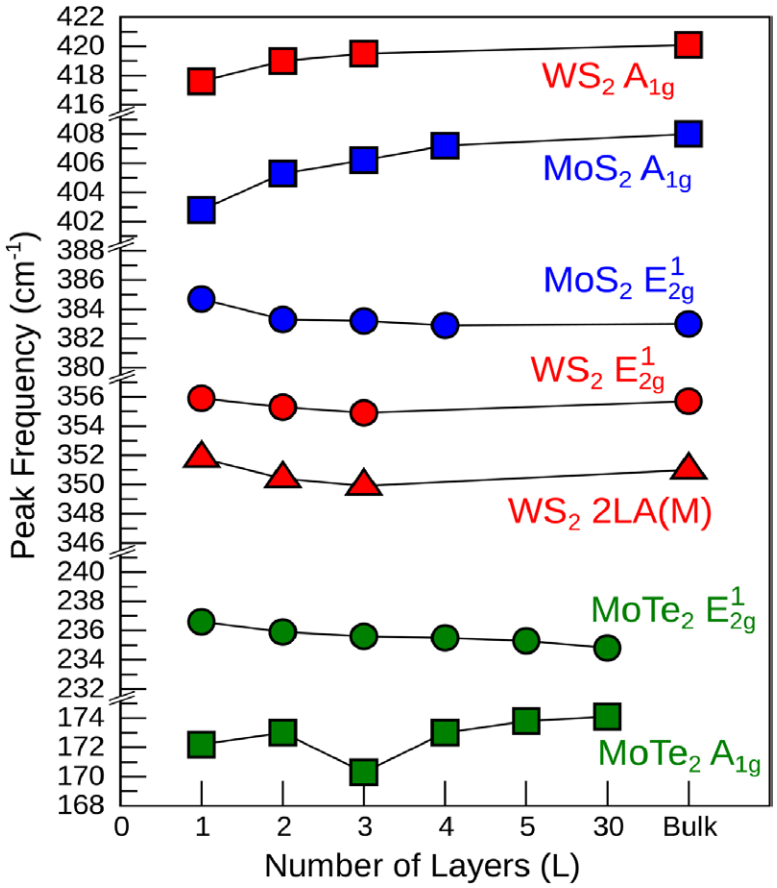

Figure 3. The number of layer (N) dependence of the frequency of the A_{1g} and E^1_{2g} Raman modes seen in MoS_2 [52], WS_2 [53] and $MoTe_2$ [55]. The 2LA mode for the M point in WS_2 is also shown. The excitation laser wavelengths used are 488 nm for MoS_2 and WS_2, and 532 nm for $MoTe_2$.

corresponds to the interlayer Raman modes locating in the low frequency region ($<100\,cm^{-1}$) of the Raman spectra. In the following text, we will describe the dependence of those Raman modes on the number of layers (section 3.2), the laser excitation wavelength (3.3) and polarization (3.4), as well as any phase transition (3.5) that have thus far been identified.

3.2. Number of layer dependence

In the layered TMDs, high-frequency intralayer Raman modes can be used to determine the number of layers N for few-layer TMDs [53, 54]. For example, the E_{2g} and A_{1g} modes undergo red and blue shifts with increasing numbers of layers for MoS_2, WS_2, $MoSe_2$, and WSe_2 [53]. Figure 3 shows the N dependence of the Raman frequency of MoS_2 [52], WS_2 [53] and $MoTe_2$ [55]. The evolution of the A_{1g} and E^1_{2g} modes shown in figure 3 which depend on the laser excitation wavelength tends to change the most between 1 and 2 layers. For WS_2, while the red shifts of the E^1_{2g} mode are within $2\,cm^{-1}$, the blue shifts of the A_{1g} mode are more obvious due to the dielectric screening effect of the vibration [56]. For few-layer MoS_2 (not shown in figure 3), the frequency differences between the E^1_{2g} and A_{1g} modes increase by $\sim 1\,cm^{-1}$ with the addition of one layer [53]. In particular, for WSe_2, the E^1_{2g} and A_{1g} modes are degenerate for the bulk material and occur at $252.2\,cm^{-1}$, but as N becomes small, the degeneracy is lifted due to symmetry breaking, leading to an additional shoulder feature that appears at 5, 6, and $11\,cm^{-1}$ above the main peak for trilayer, bilayer and monolayer WSe_2, respectively [57]. Moreover, for WSe_2, $MoSe_2$, and MoS_2, new A_{1g} modes also appear, and a splitting of the A_{1g} modes is observed for $MoSe_2$ and WS_2.

Comparing with the high-frequency intralayer Raman modes, the low-frequency interlayer Raman modes are much more sensitive to N. Zhao *et al* observed the low-frequency Raman spectra for MoS_2 and WSe_2 for $N = 1$–10 [58], in which the interlayer Raman modes monotonically change with changing N, indicating that the low-frequency interlayer Raman modes provide an optimal way to probe the N dependence of TMDs. The phonon frequencies of the interlayer Raman modes can be explained by a one-dimensional (1D) chain model in which the layers vibrate as a whole unit with mass M and a force constant K_i, (i = s, b) for the shear and breathing modes operating between the nearest neighbor units corresponding to the interlayer coupling. The frequencies of the 1D chain model behave as

$$\omega^i_p = \omega^i_0 \sin\left(\frac{P}{N}\right),\ (p = 1, \ldots, N), \tag{7}$$

where $\omega_0^i = \sqrt{K_i/M}$. The Raman active mode among the ω_p is generally the $p = 2$.

Not only do the frequencies of the interlayer Raman modes change with N, but the number of Raman active modes can also change as well. For suspended monolayer TMDs, since no interlayer coupling exists, no interlayer Raman mode is observed. For bilayer TMDs, typically there are two interlayer shear modes and one interlayer breathing mode among the interlayer modes. But the actual number of Raman modes depends on the symmetry of the modes (whether or not they are Raman active) and on the actual measurement configuration. For example, in bilayer MoS_2, only one shear mode and one breathing mode is predicted to be observed theoretically, because one interlayer shear mode is Raman inactive [59]. In some TMDs with in-plane anisotropy, such as ReS_2 and $ReSe_2$, when the incident and scattered light polarization are both along a certain crystalline axis, the intensities for some modes become zero [48, 60]. A similar case occurs for black phosphorus, another layered material with in-plane anisotropy, which shows a specific geometry that can result in a zero intensity for certain low-frequency Raman modes [57]. More discussion of these effects is given in section 3.4. With increasing N in few-layer TMDs, more interlayer shear modes and breathing modes can occur, and this is due to the increasing number of vibrational possibilities [57, 58]. For bulk TMDs, typically only one interlayer shear mode and one dominant interlayer breathing mode remain [59].

3.3. Laser excitation energy dependence

Both the frequencies and intensities of the Raman modes of TMD materials strongly depend on the laser excitation energy, E_L. As explained in the Introduction and in section 2.3, if E_L is in resonance with an exciton energy, the intensity of specific Raman modes can be enhanced significantly, which is associated with the resonance Raman effect. For example, since monolayer MoS_2 has an exciton energy around 1.8 eV, a laser energy of 633 nm laser (1.96 eV), induces a stronger Raman intensity than other common laser energy sources, such as green (532 nm) or near-infrared (785 nm) lasers. Further if the laser energy is in resonance with a 2D van Hove singularity in the joint density of states, the Raman intensity for a TMD sample is enhanced. For the hexagonal Brillouin zone (BZ) of TMD materials, a van Hove singularity appears at the center of the edge of the hexagonal BZ, which we call the M point. For example, Liu *et al* observed many overtone and combination phonon modes for monolayer MoS_2 which can be observed at E_L =3.50 eV whose intensity is even stronger than the first order Raman spectra [61]. In this case, 3.50 eV becomes the resonance energy at the M point for which the 2D van Hove singularity shows a logarithmically singular joint density of electronic states. A similar resonance effect occurs, too, in the visible light energy region for $MoTe_2$, since $MoTe_2$ has a relatively smaller energy gap [62].

Under the resonance Raman condition, not only the one-phonon Raman mode but also the two-phonon Raman modes, such as occur in the overtone or combination Raman spectra, can be observed in the double resonance Raman spectra [63, 64]. Berkdemir *et al* measured the Raman spectra of single- and few-layered WS_2 using laser excitation energies of 488, 514 and 647 nm [56]. They found that under 488 nm laser excitation, which corresponds to a non-resonant condition, only first-order Raman spectra are observed, while under the resonant condition with 514 nm laser excitation, many second-order peaks are observed and these modes show stronger intensities than those found in bulk WS_2. This situation arises because the 3D van Hove singularity in this case is not so strong compared with the other 2D van Hove singularity in WS_2 samples. Besides the intensities of the Raman modes shown in figure 3 of [56], another effect, namely that the frequencies of the Raman modes of WS_2 change slightly with a change in laser wavelength, and possible reasons are that: (1) the lattice temperature increases by strong optical absorption and (2) the photo excited carriers themselves modify the force constants of the vibration.

3.4. Polarization dependence

In section 2, we discussed the polarization dependence of the observed Raman spectra of TMD materials. The polarization dependence is useful especially for low symmetry TMDs with in-plane anisotropy, such as ReS_2 and $ReSe_2$ [28, 47, 49]. By changing the polarization direction of the incident or scattered light, the intensities of a given Raman mode are plotted as a function of the polarization direction, which is commonly done in polarized Raman spectroscopy studies. If the polar plot of Raman spectra has a maximum (or minimum) at a certain angle, we can analyze the crystalline orientation [12, 48, 57] by the group theoretical analysis as is discussed in section 2. If we simply adopt the classical theory of the Raman tensor, then the Raman tensor in equation (1) is given by specifying the symmetry of the phonon, and the polarization dependence of the Raman tensor does not change with E_L or the thickness, as far as the symmetry of the polarization does not change. However, our recent theoretical works on the study of the anisotropic Raman scattering in black phosphorus [14] and GaTe [13], indicate that special attention should also be taken when determining the crystalline orientation with polarized Raman spectroscopy, since the polarization dependence of the Raman spectra can be modified also by changing the laser excitation energy and the thickness of the sample. The reason for this unusual behavior is associated with the optical transition selection rule in the quantum theory of Raman scattering that can be expressed by the electron–photon matrix elements $\langle m|\nabla|i\rangle$ and $\langle f|\nabla|m'\rangle$ in equation (5). Since 2D TMD materials have many conduction energy bands with different symmetries at certain high-symmetry points in the Brillouin zone located over a relatively small region of energy in reciprocal space, when we change the laser energy or the thickness of the sample, the final m states in the matrix element $\langle m|\nabla|i\rangle$ can be easily shifted. It is these special final states with the different symmetries that are specially selected and this selection allows the polarization dependence of optical absorption or emission to be controlled and changed.

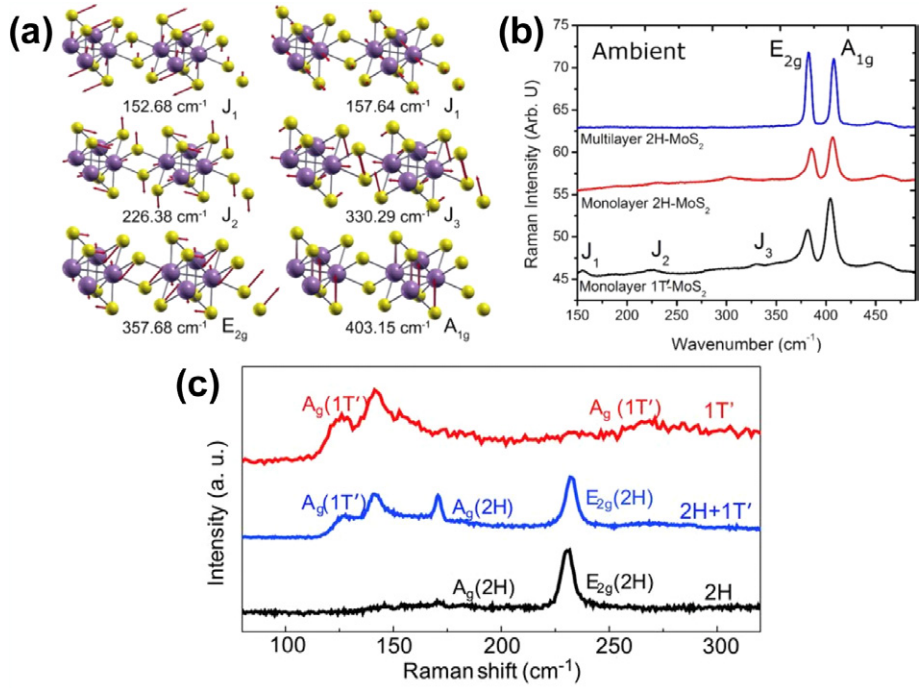

Figure 4. (a) Raman-active modes of the MoS_2 family. For the 1T′-MoS_2, the J_1 mode is composed of two Raman active modes that are close to one another and appear as one peak at room temperature [65]. Reproduced with permission from [65]. Copyright 2015 American Chemical Society; (b) Raman-active modes for the restacked monolayer 1T′-MoS_2 (black) and monolayer (red) and bulk 2H-MoS_2 (blue). The J_1, J_2, and J_3 modes are only prominent in the 1T′-MoS_2 phase [65]. Reproduced with permission from [65]. Copyright 2015 American Chemical Society; (c) Comparison of the Raman spectra of the 2H (black) and the 1T′ phase $MoTe_2$ (red). Reproduced with permission from [29]. Copyright 2015 The American Association for the Advancement of Science.

In order to get a contribution to the Raman intensity, both the $\langle m|\nabla|i\rangle$ and $\langle f|\nabla|m'\rangle$ matrix elements in equation (2) should have non-zero values, which requires the symmetry of the m and m' intermediate states to be coupled for a given initial i state. The symmetry of m and m' can be determined by the character table of the point group. As an example of this strategy, let us explain in more detail an example for studying the behavior of the E' phonon with D_{3h} symmetry as is shown in the D_{3h} character table in table 1.

When we select initial states with the symmetry A' and the polarization direction is in x and y directions (E'), the possible m for non-zero $\langle m|\nabla|i\rangle$ should have E' symmetry. Then for such an m state, possible m' states for non-zero $\langle m'|H_{el-ph}|m\rangle$ in equation (5) must have A', or A'', or E' symmetry. Among these three possible symmetries, only the E' symmetry is selected for the Raman process since we need to go back to the original initial states with A' symmetry by $\langle f|\nabla|m'\rangle$ in equation (5). Thus the symmetries of both m and m' are uniquely determined for the E' states by quantum mechanics, if we observed the E' phonon modes.

Since the electronic E' states have two independent wave functions, then $\langle m|\nabla|i\rangle$ and $\langle m'|H_{el-ph}|m\rangle$ are respectively expressed by 1×2 and 2×2 matrices. By rotating the polarization direction of light or the ∇ operator, we generally get anisotropic matrix elements both for $\langle m|\nabla|i\rangle$ and $\langle m'|H_{el-ph}|m\rangle$ as a function of the polarization dependences for a given wave function for the initial state, which can not be expressed simply by b and c parameters, as they should be given according to the classical theory. By comparing the anisotropic PL or optical absorption, the anisotropy of the electron–photon interaction for given excited states can be discussed, which will be done in a future study.

3.5. Phase transitions of TMDs

As introduced before, TMDs can undergo phase transitions between 2H, 3R, 1T and 1T′ phases. Raman spectroscopy has big advantages in distinguishing the various phases of TMDs, through measuring distinct Raman intensity and frequencies for each phase by changing the laser excitation energy, pressure and temperature. Cho *et al* reported that semiconducting 2H-$MoTe_2$ can make a transition to the semi-metallic 1T′-$MoTe_2$ phase by laser-irradiation [29]. Kappera *et al* [62] and Nayak *et al* [30] reported that the 2H-MoS_2 can make a transition to the metallic 1T-MoS_2 phase through a *n*-butyl lithium chemical treatment. Since both the 1T or 1T′ phases of MoS_2 are metallic, while the 2H phase is semiconducting, intense attention has been paid to fabricate ohmic homojunction contact of a transistor using the 1T (or 1T′) phase to the 2H phase of the same TMD for both the devices and for the electrical circuit contacts [27, 32, 65]. It should be noted that additional Raman peaks are observed for the 1T (or 1T′) phase compared to the 2H phase as shown in figure 4(c). For example, 1T′-MoS2 has additional peaks denoted by J_1, J_2, and J_3 in the bottom of figure 4(b) at 153, 226, 330 cm^{-1}, respectively, whose eigenvectors are shown in figure 4(a) [65]. Similarly, the 2H-$MoTe_2$ exhibits only E_{2g} and A_g modes at 235 cm^{-1} and 174 cm^{-1}, respectively, while the 1T′-$MoTe_2$ does not

clearly show the E_{2g} mode but new peaks near 124, 138, and 272 cm^{-1} are instead observed (figure 4(c)) [29]. The appearance of the new peaks comes from the fact that the 1T′ phase has relatively lower in-plane symmetry than the 2H phase.

4. Raman spectra of TMD heterostructures

In this section, we discuss the Raman spectra of TMD heterostructures. By stacking two layers of different TMDs together, we can obtain new heterostructures made of TMDs that are not found in natural crystals. When the two layers are of the same material, we can get so-called twisted bilayer TMDs by rotating one TMD layer relative to another layer along the axis perpendicular to the TMD plane. Designing heterostructures of TMD materials has become a popular trend nowadays, because the heterojunction applications enabled by such semiconductor heterostructures offer a vast number of possibilities for both fundamental and applications research [66–71]. The band offset effect, especially occurring in the type II heterojunction [67–70, 72], enables the preparation of many devices with much better performances than have been observed with devices made with a single material, such as p–n junctions, highly efficient LEDs [73], solar cells [67, 74] and tunneling FETs [75, 76] that can be achieved using heterojunctions, such as WSe_2/MoS_2 and $WSe_2/MoSe_2$, etc. It should be noted that the idea of a heterojunction dates back more than 80 years ago [77], when a 2D material was considered as a non-existing one. Later, in the 1970s, heterojunctions were realized experimentally, using semiconductor superlattices, such as GaAs/AlAs and HgTe/CdTe [78, 79] where the importance of lattice matching was emphasized. These superlattices, constructed with very thin layers of materials, were considered quasi-2D at that time. The recent study of heterostructures of 2D materials reveals new physics about possible heterojunctions of 'true' 2D materials and the unique physics regarding electron transport, and optoelectronic transitions in such materials, thereby opening a new route for both fundamental study and device research as well [66].

In this section, we first discuss twisted bilayer TMD (schematically shown in figure 5(a)). We then present the unique physics of twisted bilayers of the same TMD and the characterization of them by PL and Raman spectroscopy. Then, we explain twisted TMD heterobilayers, (schematically shown in figure 5(b)), and we finally show some examples, too.

4.1. Twisted bilayer TMD

A twisted bilayer TMD is a special case of a heterostructure. For twisted bilayer TMD, the two layers consist of the same material, but due to the twisting between them, their interlayer coupling is dramatically changed compared to the naturally stacked TMDs, and such interlayer coupling plays a crucial role in the electronic and optical properties of twisted bilayer TMDs. Here we present the case of twisted bilayer MoS_2 (schematically illustrated in figure 5(a)), and this example can be used as a standard reference material for TMDs, and the concepts developed for twisted MoS_2 can be generalized to other twisted heterobilayer TMDs.

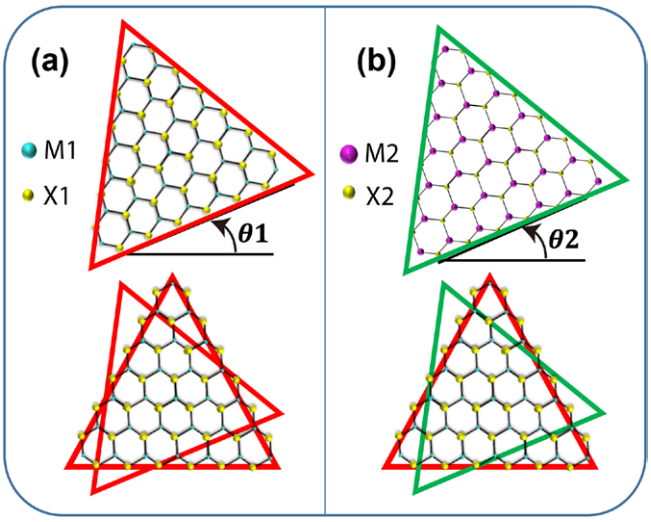

Figure 5. Schematic illustrations of (a) a twisted bilayer TMD and (b) a heterobilayer TMDs.

The twisted MoS_2 bilayer is synthesized by a single crystal flake which can be made experimentally by the CVD-grown monolayer process for MoS_2 with a triangle shape [2], and by using a so-called dry transfer method, by which the two layers are stacked onto each other through the manipulation of a micro-stage and an optical microscope [80]. Therefore, the twisting angle is easily controlled by an optical microscope, as shown in figure 6(a). Such a dry transfer method avoids introduction of foreign substances in between the two layers of MoS_2, and therefore, the best interlayer coupling is achieved by this method.

The interlayer coupling of 2H stacked MoS_2 is relatively strong, due to the p_z orbitals of the *S* atoms which stretch out well beyond the single layer and interact with the *S* atoms of the adjacent layer. Therefore, from a monolayer to a bilayer, the electronic properties of 2H MoS_2 change dramatically: the band gap changes from direct to indirect, and the photoluminescence (PL) quantum yield drops by a factor of more than 100 [30]. These applications and PL intensity ratios can be used to characterize the quality of the 2H-MoS_2 bilayer that is formed.

Similar to 2H-stacked bilayer MoS_2, twisted bilayer MoS_2 also has a much smaller photoluminescence intensity than a monolayer [80], which also confirms the weaker PL intensity coming from the bilayer area than from the monolayer area. A similar phenomenon occurs in 2H stacked MoS_2. In a control experiment, we built a twisted bilayer MoS_2 sample with the wet transfer method which introduces trace amounts of PMMA residues between the two layers of MoS_2, and the resulting photoluminescence spectra show bilayer areas that are not well coupled because they have stronger PL intensity than the monolayer area.

Low-frequency Raman spectra can further characterize twisted bilayer MoS_2 [59] and are also sensitive to the interlayer coupling of layered materials. Nayak *et al* observed [62] the interlayer shear mode and breathing mode of twisted bilayer MoS_2 as shown in figure 6(a). As reported from the literature for bilayer MoS_2, the interlayer shear mode is at ~23 cm^{-1}

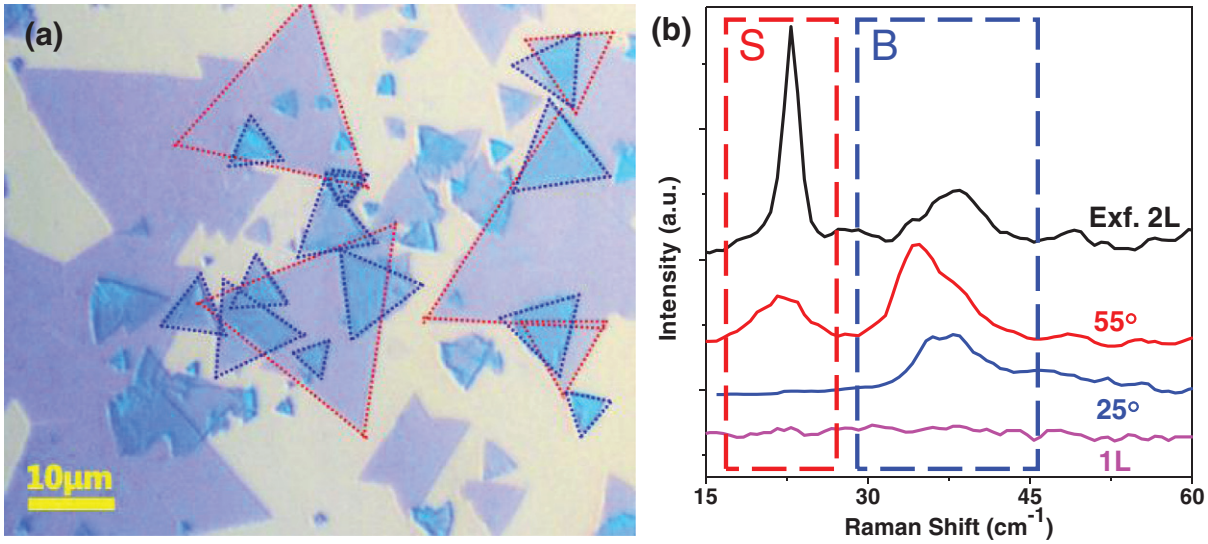

Figure 6. (a) An optical microscope image of twisted bilayer MoS_2. (b) Low frequency (interlayer) Raman spectra of twisted bilayer MoS_2 with twisting angles of 55° and 25°, as well as of exfoliated bilayer MoS_2 with 2H stacking, and of monolayer (1L) MoS_2 [59]. Reproduced with permission from [59]. Copyright 2016 American Chemical Society.

and the interlayer breathing mode is at ~36 cm^{-1} [58]. The twisted bilayer MoS_2, on the other hand, has interlayer breathing and shear modes that are highly sensitive to variation of the twist angle. For example, the interlayer shear mode can be observed in bilayer MoS_2 with a twist angle with $\theta = 55°$, but not with a twist angle of 25° (see figure 6(b)). In fact, when the twisting angle is close to 30°, the interlayer coupling becomes very weak, and thus shear modes are not observed [59]. Combined with DFT calculations, it turns out that the interlayer shear mode in such a case gives a very low frequency (1–2 cm^{-1}), which suggests a 100 times smaller interlayer shear force than that for 2H stacked MoS_2 [59], and this result was confirmed by experimental observation [81]. Exfoliated 2H stacked bilayer MoS_2 shows stronger interlayer shear modes than the twisted bilayers. The shear mode frequency can vary by around 8 cm^{-1} with several twisting angles, and the intensity can vary by around a factor of 5. Such a large degree of sensitivity cannot occur in the high-frequency Raman modes of MoS_2, since their variation in frequency with twist is no more than 1 cm^{-1}.

Similar phenomena for the low-frequency Raman modes were observed in twisted bilayer $MoSe_2$ [82], and were explained by a combination of the high-symmetry stackings with different twisting angles. Moreover, CVD-grown bilayer and trilayer TMDs with different stacking configurations (2H, 3R, etc) were studied by low-frequency Raman spectroscopy [83], and it was found that low-frequency Raman spectroscopy is sensitive to stacking patterns, while the high-frequency Raman spectra yield the same spectra for different stacking configurations, because they are generally not sensitive to such small percentage changes.

Except for the low-frequency Raman modes, the PL parameters also change by changing twisting angles. The PL spectrum of monolayer MoS_2 consists of three peaks: A-, A and B, which represent the A- trion (doped exciton by an additional electron or hole), the A exciton and the B exciton, respectively [80, 84]. The intensity ratio I_{A^-}/I_A shows a dependence on twisting angles: the maximum intensity value occurs at 0° and 60°, and a minimum value at 30°. The trion binding energy witnesses a similar trend: the maximum binding energy around 55 meV occurs at 0° and 60°, and a minimum at 30 meV occurring at around 30°. These results for the change in the interlayer coupling with twisting angle θ_t were confirmed by the DFT calculations [80]. In some other works, the indirect PL peaks of twisted bilayer MoS_2 were studied [85, 86], in which a PL peak between around 1.4 eV–1.6 eV shows up experimentally, and is demonstrated to be caused by an indirect band gap due to the presence of bilayer MoS_2, which changes with different twisting angles (different interlayer coupling) and results in the tuning of the PL peak positions.

From the above analyses of twisted bilayer TMD, we can see that low-frequency Raman and PL spectroscopies are very sensitive ways to probe the interlayer coupling of layered TMD materials, and these sensitivities can be utilized in the practical applications and device research [67, 70–73, 76, 87].

4.2. TMD hetero bilayers

The TMD hetero bilayers are built to achieve different kinds of devices for various applications. Generally, dry-transfer and CVD growth [2, 88] are two ways to construct TMD hetero bilayers. While the dry-transfer method is limited to produce vertically stacked hetero bilayers only, the CVD growth is able to generate parallel-stitching of TMD materials, resulting in in-plane heterojunction [68, 69, 88–90]. As a first check of the device performance, low-frequency Raman spectroscopy can be used to characterize the interlayer coupling of vertically stacked hetero bilayers. Several works have been performed to study this. For example, Lui *et al* [79] built several types of heterobilayer TMDs and characterized them by low frequency Raman spectroscopy. They showed that the low-frequency Raman spectra are mainly the breathing mode as a combination of the two constituent materials, but that the shearing

mode disappears in most cases [81]. This is because the shear mode requires the relative shear motion for the entire layers of the hetero structure to move in the direction parallel to the layers, and thus the shear force with a lattice-mismatched hetero structure can be negligibly small. Such a shear force for the lattice-mismatched heterostructure occurs within a relatively short distance compared with the sample size, and can only be of significant magnitude when the interlayer coupling is strong enough. Such a low frequency shear mode is hard to detect experimentally, due to the limitations of a strong Rayleigh spectra [59]. DFT calculations also demonstrated that the interlayer shear mode is much more sensitive to interlayer coupling or to the interlayer separation distance than the interlayer breathing modes [59]. On the other hand, for the interlayer breathing modes, the relative motions between the layers are vertical, and such force constants for vertically motion are less sensitive to the lattice hetero structure mismatch. Thus we mainly observe experimentally the interlayer breathing modes of heterobilayers.

The high-frequency Raman spectra are also useful to characterize parallel heterojunctions. For example, we measured Raman mapping for the high frequency mode around the junction area from which we confirm that the heterojunction is in-plane [88], because there are no overlapping Raman signals coming from the two materials simultaneously. On the other hand, the high-frequency Raman spectra can be used to characterize the strain in the materials close to the junction area, since these Raman modes are sensitive to strain [89].

Moreover, several heterojunctions have been constructed for the study of interlayer PL, which shows different mechanisms for the optical transition at the junction from the traditional PL. A typical example of the interlayer PL is that the hetero junction of 2D TMDs exhibits direct optical transitions of electrons from one material to another material [73, 91]. Rivera *et al* show that the interlayer excitons are found to exhibit long lifetimes compared with the exciton coming from bulk materials [71]. The peak position of the PL spectra from the junction is shifted from the PL spectra of the constituent two materials. Such studies of the PL emissions in TMD hetero bilayers can lead to both new optoelectronic devices and characterization tools for hetero bilayers.

The above analyses and Raman spectroscopy for both twisted bilayer TMDs, homojunctions and heterojunctions of TMDs can benefit similar studies on other 2D materials, such as graphene [92] and black phosphorus [87]. By combining the new science coming from characterization studies for all systems, Raman spectroscopy can provide a standard tool for characterizing the interlayer coupling and junction properties of hetero structure TMDs for obtaining measurements from high quality optoelectronic devices.

5. Summary and perspective

With the wide variety of structures and phases presently available for TMD materials, the research community can already see that TMD materials can obtain various electronic and optical properties enabling their applications in different areas of fundamental scientific research and for new applications capabilities at the nanoscale. From the viewpoint of fundamental research, Raman spectroscopy is becoming a common and standard tool for probing the properties of layered materials. Pure TMDs are becoming a class of standard reference materials for well-defined 2D layered materials with a bandgap. Thus combining TMD materials into a new artificial material is expected to provide new possibilities for electronics applications.

We here consider MoS_2 as being a TMD standard reference material, analogous to the role of graphene, which is a standard reference material for single-layer constituents in most 2D layer hetero structure assemblies not found in nature, but capable of offering device applications not available presently. We can expect this TMD material MoS_2 to be followed by a whole family of new materials and their hetero structured systems with different levels of complexity as they are combined. After TMDs, more complex systems are expected. Such materials systems are now under investigation and include low-symmetry systems with only one or two available symmetry operations. Such systems are also found in nature and may become more important once we know more about them and their unique advantages for different types of applications.

In this article we have provided a systematic discussion of the Raman spectra of TMDs, giving particular attention to the control of TMD properties as classical layered materials. Here control of the properties of the whole class of materials comes, as in all cases, from the control of the properties of the individual fundamental building block layers. Additional control comes through the change in properties coming from increasing the number of layers, one by one at first, and then use of possible stable phases of the fundamental materials. Further control comes from use of different laser excitation energy wavelengths, looking for resonance behaviors from a quantum mechanical standpoint, and then when assembling multilayer structures of more than one material. Many variations are possible through exploitation of materials parameters such as layer thickness, structural phases and phase transitions, excitation laser wavelengths, including very long wavelengths or low frequency excitations and polarization-dependent characteristics. In addition, use can be made of variations coming from commonly used parameters of temperature, pressure, stress, pressure, magnetic and electric fields, and materials processing characteristics. This large number of variables can be further increased by using more than one building block together, thereby giving us a large phase space for operation and the exploration of new environments for our nanomaterial heterostructures. This research landscape offers great complexity because the appropriate variables for each of the constituents in the heterostructures that are somewhat independent, though the layers need to be assembled in a way as to be mutually compatible chemically.

Our goal is both to find new scientific phenomena occurring at the nanoscale through these heterostructures not found in natural nanostructured materials, and to identify the structures and environments of particular promise and interest for science and for applications. The next step is to pursue the new science and to develop opto-electronic devices in two

dimensions. At this point, new variables enter, such as safety in production and use, cost of materials and their processing, long term stability, materials availability, and possible commercial interest. At the research and applications level, nano heterostructures are likely to become more complex with time. Studies of fundamental scientific interest going beyond the model systems will have to be carried out and we will be excited whenever new scientific ideas are identified through these studies and also when sensitive methods are found to control more effectively the fruitful research directions that have already been identified.

Acknowledgments

RS acknowledges MEXT grant (No. 25107005). YT acknowledges the MD program of Tohoku University. SH, XL, and MSD acknowledge National Science Foundation (XL, MSD) grant 2DARE (EFRI-1542815) and the US Department of Energy (SH, MSD) grant DE-SC0001299 for financial support.

References

[1] Novoselov K S, Geim a K, Morozov S V, Jiang D, Zhang Y, Dubonos S V, Grigorieva I V and Firsov A A 2004 Electric field effect in atomically thin carbon films *Science* **306** 666–9
[2] Ling X, Lee Y-H, Lin Y, Fang W, Yu L, Dresselhaus M S and Kong J 2014 Role of the seeding promoter in MoS_2 growth by chemical vapor deposition *Nano Lett.* **14** 464–72
[3] Saito R, Hofmann M, Dresselhaus G, Jorio A and Dresselhaus M S 2011 Raman spectroscopy of graphene and carbon nanotubes *Adv. Phys.* **60** 413–550
[4] Jorio A, Saito R, Dresselhaus G and Dresselhaus M S 2011 *Raman Spectroscopy in Graphene Related Systems* (New York: Wiley)
[5] Dresselhaus M S, Jorio A and Saito R 2010 Characterizing graphene, graphite, and carbon nanotubes by Raman spectroscopy *Annu. Rev. Condens. Matter Phys.* **1** 89–108
[6] Dresselhaus M S, Jorio A, Hofmann M, Dresselhaus G and Saito R 2010 Perspectives on carbon nanotubes and graphene Raman spectroscopy *Nano Lett.* **10** 751–8
[7] Zhang X, Qiao X-F, Shi W, Wu J-B, Jiang D-S and Tan P-H 2015 Phonon and Raman scattering of 2D transition metal dichalcogenides from monolayer, multilayer to bulk material *Chem. Soc. Rev.* **44** 2757–85
[8] Molina-Sánchez A, Hummer K and Wirtz L 2015 Vibrational and optical properties of MoS_2: from monolayer to bulk *Surf. Sci. Rep.* **70** 554–86
[9] Souza Filho A G *et al* 2004 Stokes and anti-stokes Raman spectra of small-diameter isolated carbon nanotubes *Phys. Rev.* B **69** 115428
[10] Roldán R, Castellanos-Gomez A, Cappelluti E and Guinea F 2015 Strain engineering in semiconducting 2D crystals *J. Phys.: Condens. Matter* **27** 313201
[11] Cong C, Yu T, Sato K, Shang J, Saito R, Dresselhaus G F and Dresselhaus M S 2011 Raman characterization of ABA- and ABC-stacked trilayer graphene *ACS Nano* **5** 8760–8
[12] Pimenta M A, Dresselhaus G, Dresselhaus M S, Cançado L G, Jorio A and Saito R 2007 Studying disorder in graphite-based systems by Raman spectroscopy *Phys. Chem. Chem. Phys.* **9** 1276–90
[13] Huang S *et al* 2016 In-plane anisotropic optical spectroscopy of layered gallium telluride *Nano Lett.* at press
[14] Ling X *et al* 2016 Anisotropic electron–photon and electron–phonon interactions in black phosphorus *Nano Lett.* **16** 2260–7
[15] Loudon R 1964 The Raman effect in crystals *Adv. Phys.* **13** 423–82
[16] Cardona M 1983 *Light Scattering in Solids I* vol 8 (Berlin: Springer)
[17] Dresselhaus M S, Dresselhaus G and Jorio A 2008 *Group Theory: Application to the Physics of Condensed Matter* (Berlin: Springer)
[18] Sakurai J J and Napolitano J J 2011 *Modern Quantum Mechanics* (Reading, MA: Addison-Wesley)
[19] Grüneis A, Saito R, Samsonidze G G, Kimura T, Pimenta M A, Jorio A, Filho A G S, Dresselhaus G and Dresselhaus M S 2003 Inhomogeneous optical absorption around the *K* point in graphite and carbon nanotubes *Phys. Rev.* B **67** 165402
[20] Wilson J A and Yoffe A D 1969 The transition metal dichalcogenides discussion and interpretation of the observed optical, electrical and structural properties *Adv. Phys.* **18** 193–335
[21] Ribeiro-Soares J, Almeida R M, Barros E B, Araujo P T, Dresselhaus M S, Cançado L G and Jorio A 2014 Group theory analysis of phonons in 2D transition metal dichalcogenides *Phys. Rev.* B **90** 115438
[22] Lv R, Terrones H, Elías A L, Perea-López N, Gutiérrez H R, Cruz-Silva E, Rajukumar L P, Dresselhaus M S and Terrones M 2015 2D transition metal dichalcogenides: clusters, ribbons, sheets and more *Nano Today* **10** 559–92
[23] Terrones H *et al* 2014 New first order Raman-active modes in few layered transition metal dichalcogenides *Sci. Rep.* **4** 4215
[24] Molina-Sánchez A and Wirtz L 2011 Phonons in single-layer and few-layer MoS_2 and WS_2 *Phys. Rev.* B **84** 155413
[25] Whitesides G M, Aizenberg J and Black A J 1999 Control of crystal nucleation by patterned self-assembled monolayers *Nature* **398** 495–8
[26] Wang Q H, Kalantar-Zadeh K, Kis A, Coleman J N and Strano M S 2012 Electronics and optoelectronics of 2D transition metal dichalcogenides *Nat. Nanotechnol.* **7** 699–712
[27] Duerloo K-A N, Li Y and Reed E J 2014 Structural phase transitions in 2D Mo- and W-dichalcogenide monolayers *Nat. Commun.* **5** 4214
[28] Keum D H *et al* 2015 Bandgap opening in few-layered monoclinic $MoTe_2$ *Nat. Phys.* **11** 482–6
[29] Cho S *et al* 2015 Phase patterning for ohmic homojunction contact in $MoTe_2$ *Science* **349** 625–8
[30] Mak K F, Lee C, Hone J, Shan J and Heinz T F 2010 Atomically thin MoS_2: a new direct-gap semiconductor *Phys. Rev. Lett.* **105** 136805
[31] Liu G-B, Xiao D, Yao Y, Xu X and Yao W 2015 Electronic structures and theoretical modelling of 2D group-VIB transition metal dichalcogenides *Chem. Soc. Rev.* **44** 2643–63
[32] Kappera R, Voiry D, Yalcin S E, Branch B, Gupta G, Mohite A D and Chhowalla M 2014 Phase-engineered low-resistance contacts for ultrathin MoS_2 transistors *Nat. Mater.* **13** 1128–34
[33] Huang Y, Xu K, Wang Z, Shifa T A, Wang Q, Wang F, Jiang C and He J 2015 Designing the shape evolution of $SnSe_2$ nanosheets and their optoelectronic properties *Nanoscale* **7** 17375–80
[34] Yu X, Zhu J, Zhang Y, Weng J, Hu L and Dai S 2012 $SnSe_2$ quantum dot sensitized solar cells prepared employing molecular metal chalcogenide as precursors *Chem. Commun.* **48** 3324
[35] Wang R Y, Caldwell M A, Jeyasingh R G D, Aloni S, Shelby R M, Wong H-S P and Milliron D J 2011 Electronic

and optical switching of solution-phase deposited $SnSe_2$ phase change memory material *J. Appl. Phys.* **109** 113506
[36] Choi J, Jin J, Jung I G, Kim J M, Kim H J and Son S U 2011 $SnSe_2$ nanoplate-graphene composites as anode materials for lithium ion batteries *Chem. Commun.* **47** 5241
[37] Zhang C, Yin H, Han M, Dai Z, Pang H, Zheng Y, Lan Y-Q, Bao J and Zhu J 2014 2D tin selenide nanostructures for flexible all-solid-state supercapacitors *ACS Nano* **8** 3761–70
[38] Bovet M, Popović D, Clerc F, Koitzsch C, Probst U, Bucher E, Berger H, Naumović D and Aebi P 2004 Pseudogapped Fermi surfaces of 1T–TaS_2 and 1T–$TaSe_2$: a charge density wave effect *Phys. Rev.* B **69** 125117
[39] Xu K, Chen P, Li X, Wu C, Guo Y, Zhao J, Wu X and Xie Y 2013 Ultrathin nanosheets of vanadium diselenide: a metallic 2D material with ferromagnetic charge-density-wave behavior *Angew. Chem. Int. Ed.* **52** 10477–81
[40] Kačmarčík J, Pribulová Z, Marcenat C, Klein T, Rodière P, Cario L and Samuely P 2010 Specific heat measurements of a superconducting NbS_2 single crystal in an external magnetic field: energy gap structure *Phys. Rev.* B **82** 014518
[41] Leroux M, Le Tacon M, Calandra M, Cario L, Méasson M-A, Diener P, Borrissenko E, Bosak A and Rodière P 2012 Anharmonic suppression of charge density waves in 2H-NbS_2 *Phys. Rev.* B **86** 155125
[42] Leroux M, Rodière P, Cario L and Klein T 2012 Anisotropy and temperature dependence of the first critical field in 2H-NbS_2 *Phys. B: Condens. Matter* **407** 1813–5
[43] Huang Y H, Peng C C, Chen R S, Huang Y S and Ho C H 2014 Transport properties in semiconducting NbS_2 nanoflakes *Appl. Phys. Lett.* **105** 093106
[44] Liu Z-L, Cai L-C and Zhang X-L 2014 Novel high pressure structures and superconductivity of niobium disulfide *J. Alloys Compd.* **610** 472–7
[45] Corbet C M, McClellan C, Rai A, Sonde S S, Tutuc E and Banerjee S K 2015 Field effect transistors with current saturation and voltage gain in ultrathin ReS_2 *ACS Nano* **9** 363–70
[46] Tongay S *et al* 2014 Monolayer behaviour in bulk ReS_2 due to electronic and vibrational decoupling *Nat. Commun.* **5** 3252
[47] Wolverson D, Crampin S, Kazemi A S, Ilie A and Bending S J 2014 Raman spectra of monolayer, few-layer, and bulk $ReSe_2$: an anisotropic layered semiconductor *ACS Nano* **8** 11154–64
[48] Zhao H, Wu J, Zhong H, Guo Q, Wang X, Xia F, Yang L, Tan P and Wang H 2015 Interlayer interactions in anisotropic atomically thin rhenium diselenide *Nano Res.* **8** 3651–61
[49] Chenet D A, Aslan O B, Huang P Y, Fan C, van der Zande A M, Heinz T F and Hone J C 2015 In-plane anisotropy in mono- and few-layer ReS_2 probed by Raman spectroscopy and scanning transmission electron microscopy *Nano Lett.* **15** 5667–72
[50] Ho C H, Huang Y S and Tiong K K 2001 In-plane anisotropy of the optical and electrical properties of ReS_2 and $ReSe_2$ layered crystals *J. Alloys Compd.* **317–8** 222–6
[51] Ho C H and Huang C E 2004 Optical property of the near band-edge transitions in rhenium disulfide and diselenide *J. Alloys Compd.* **383** 74–9
[52] Friemelt K, Lux-Steiner M-C and Bucher E 1993 Optical properties of the layered transition-metal-dichalcogenide ReS_2: anisotropy in the van der Waals plane *J. Appl. Phys.* **74** 5266
[53] Li H, Zhang Q, Yap C C R, Tay B K, Edwin T H T, Olivier A and Baillargeat D 2012 From bulk to monolayer MoS_2: evolution of Raman scattering *Adv. Funct. Mater.* **22** 1385–90
[54] Lee C, Yan H, Brus L E, Heinz T F, Hone J and Ryu S 2010 Anomalous lattice vibrations of single- and few-layer MoS_2 *ACS Nano* **4** 2695–700
[55] Yamamoto M, Wang S T, Ni M, Lin Y-F, Li S-L, Aikawa S, Jian W-B, Ueno K, Wakabayashi K and Tsukagoshi K 2014 Strong enhancement of Raman scattering from a bulk-inactive vibrational mode in few-layer $MoTe_2$ *ACS Nano* **8** 3895–903
[56] Berkdemir A *et al* 2013 Identification of individual and few layers of WS_2 using Raman spectroscopy *Sci. Rep.* **3** 1755
[57] Sahin H, Tongay S, Horzum S, Fan W, Zhou J, Li J, Wu J and Peeters F M 2013 Anomalous Raman spectra and thickness-dependent electronic properties of WSe_2 *Phys. Rev.* B **87** 165409
[58] Zhao Y *et al* 2013 Interlayer breathing and shear modes in few-trilayer MoS_2 and WSe_2 *Nano Lett.* **13** 1007–15
[59] Huang S, Liang L, Ling X, Puretzky A A, Geohegan D B, Sumpter B G, Kong J, Meunier V and Dresselhaus M S 2016 Low-frequency interlayer Raman modes to probe interface of twisted bilayer MoS_2 *Nano Lett.* **16** 1435–44
[60] He R, Yan J-A, Yin Z, Ye Z, Ye G, Cheng J, Li J and Lui C H 2016 Coupling and stacking order of ReS_2 atomic layers revealed by ultralow-frequency Raman spectroscopy *Nano Lett.* **16** 1404–9
[61] Liu H-L, Guo H, Yang T, Zhang Z, Kumamoto Y, Shen C-C, Hsu Y-T, Li L-J, Saito R and Kawata S 2015 Anomalous lattice vibrations of monolayer MoS_2 probed by ultraviolet Raman scattering *Phys. Chem. Chem. Phys.* **17** 14561–8
[62] Guo H, Yang T, Yamamoto M, Zhou L, Ishikawa R, Ueno K, Tsukagoshi K, Zhang Z, Dresselhaus M S and Saito R 2015 Double resonance Raman modes in monolayer and few-layer $MoTe_2$ *Phys. Rev.* B **91** 205415
[63] Saito R *et al* 2003 Double resonance Raman spectroscopy of single-wall carbon nanotubes *New J. Phys.* **5** 157
[64] Saito R, Jorio A, Souza Filho A G, Dresselhaus G, Dresselhaus M S and Pimenta M A 2001 Probing phonon dispersion relations of graphite by double resonance Raman scattering *Phys. Rev. Lett.* **88** 027401
[65] Nayak A P *et al* 2015 Pressure-dependent optical and vibrational properties of monolayer molybdenum disulfide *Nano Lett.* **15** 346–53
[66] Geim A K and Grigorieva I V 2013 Van der Waals heterostructures *Nature* **499** 419–25
[67] Furchi M M, Pospischil A, Libisch F, Burgdörfer J and Mueller T 2014 Photovoltaic effect in an electrically tunable van der Waals heterojunction *Nano Lett.* **14** 4785–91
[68] Huang C, Wu S, Sanchez A M, Peters J J P, Beanland R, Ross J S, Rivera P, Yao W, Cobden D H and Xu X 2014 Lateral heterojunctions within monolayer $MoSe_2$–WSe_2 semiconductors *Nat. Mater.* **13** 1096–101
[69] Zhang C, Chen Y, Huang J-K, Wu X, Li L-J, Yao W, Tersoff J and Shih C-K 2016 Visualizing band offsets and edge states in bilayer–monolayer transition metal dichalcogenides lateral heterojunction *Nat. Commun.* **7** 10349
[70] Chiu M-H, Zhang C, Shiu H-W, Chuu C-P, Chen C-H, Chang C-Y S, Chen C-H, Chou M-Y, Shih C-K and Li L-J 2015 Determination of band alignment in the single-layer MoS_2/WSe_2 heterojunction *Nat. Commun.* **6** 7666
[71] Rivera P *et al* 2015 Observation of long-lived interlayer excitons in monolayer $MoSe_2$–WSe_2 heterostructures *Nat. Commun.* **6** 6242
[72] Nourbakhsh A, Zubair A, Dresselhaus M S and Palacios T 2016 Transport properties of a MoS_2/WSe_2 heterojunction transistor and its potential for application *Nano Lett.* **16** 1359–66
[73] Lee C-H *et al* 2014 Atomically thin p–n junctions with van der Waals heterointerfaces *Nat. Nanotechnol.* **9** 676–81
[74] Bernardi M, Palummo M and Grossman J C 2013 Extraordinary sunlight absorption and one nanometer thick photovoltaics using 2D monolayer materials *Nano Lett.* **13** 3664–70

[75] Roy T, Tosun M, Cao X, Fang H, Lien D-H, Zhao P, Chen Y-Z, Chueh Y-L, Guo J and Javey A 2015 Dual-gated MoS_2/WSe_2 van der Waals tunnel diodes and transistors *ACS Nano* **9** 2071–9
[76] Yan R *et al* 2015 Esaki diodes in van der Waals heterojunctions with broken-gap energy band alignment *Nano Lett.* **15** 5791–8
[77] Bradley A J and Jay A H 1932 The formation of superlattices in alloys of iron and aluminium on JSTOR *Proc. R. Soc.* A **136** 210–32
[78] Esaki L and Tsu R 1970 Superlattice and negative differential conductivity in semiconductors *IBM J. Res. Dev.* **14** 61–5
[79] Esaki L and Chang L L 1974 New transport phenomenon in a semiconductor 'superlattice' *Phys. Rev. Lett.* **33** 495–8
[80] Huang S, Ling X, Liang L, Kong J, Terrones H, Meunier V and Dresselhaus M S 2014 Probing the interlayer coupling of twisted bilayer MoS_2 using photoluminescence spectroscopy *Nano Lett.* **14** 5500–8
[81] Lui C H *et al* 2015 Observation of interlayer phonon modes in van der Waals heterostructures *Phys. Rev.* B **91** 165403
[82] Puretzky A A, Liang L, Li X, Xiao K, Sumpter B G, Meunier V and Geohegan D B 2016 Twisted $MoSe_2$ bilayers with variable local stacking and interlayer coupling revealed by low-frequency raman spectroscopy *ACS Nano* **10** 2736
[83] Puretzky A A *et al* 2015 Low-frequency raman fingerprints of 2D metal dichalcogenide layer stacking configurations *ACS Nano* **9** 6333–42
[84] Mak K F, He K, Lee C, Lee G H, Hone J, Heinz T F and Shan J 2013 Tightly bound trions in monolayer MoS_2 *Nat. Mater.* **12** 207–11
[85] van der Zande A M *et al* 2014 Tailoring the electronic structure in bilayer molybdenum disulfide via interlayer twist *Nano Lett.* **14** 3869–75
[86] Liu K, Zhang L, Cao T, Jin C, Qiu D, Zhou Q, Zettl A, Yang P, Louie S G and Wang F 2014 Evolution of interlayer coupling in twisted molybdenum disulfide bilayers *Nat. Commun.* **5** 4966
[87] Deng Y, Luo Z, Conrad N J, Liu H, Gong Y, Najmaei S, Ajayan P M, Lou J, Xu X and Ye P D 2014 Black phosphorus–monolayer MoS_2 van der Waals heterojunction p–n diode *ACS Nano* **8** 8292–9
[88] Ling X *et al* 2016 Parallel stitching of 2D materials *Adv. Mater.* **28** 2322–9
[89] Li M-Y *et al* 2015 Epitaxial growth of a monolayer WSe_2–MoS_2 lateral p–n junction with an atomically sharp interface *Science* **349** 524–8
[90] Mahjouri-Samani M *et al* 2015 Patterned arrays of lateral heterojunctions within monolayer 2D semiconductors *Nat. Commun.* **6** 7749
[91] Cheng R, Li D, Zhou H, Wang C, Yin A, Jiang S, Liu Y, Chen Y, Huang Y and Duan X 2014 Electroluminescence and photocurrent generation from atomically sharp WSe_2 / MoS_2 heterojunction p–n diodes *Nano Lett.* **14** 5590–7
[92] Roy K, Padmanabhan M, Goswami S, Sai T P, Ramalingam G, Raghavan S and Ghosh A 2013 Graphene-MoS_2 hybrid structures for multifunctional photoresponsive memory devices *Nat. Nanotechnol.* **8** 826–30